Soft Matter

Molecular simulations of the piezoionic effect

Journal:	*Soft Matter*
Manuscript ID	SM-ART-05-2018-000939.R2
Article Type:	Paper
Date Submitted by the Author:	28-Jun-2018
Complete List of Authors:	Triandafilidi, Vasilii; Univerisity of British Columbia, Chemical and Biological Engineering Hatzikiriakos, Savvas; The University of British Columbia, Chemical and Biological Engineering Rottler, Jörg; The University of British Columbia, Department of Physics and Astronomy

Soft Matter

ARTICLE TYPE

Cite this: DOI: 10.1039/xxxxxxxxxx

Molecular simulations of the piezoionic effect

Vasilii Triandafilidi,*[a] Savvas Hatzikiriakos,[a] and Jörg Rottler[b]

Received Date
Accepted Date

DOI: 10.1039/xxxxxxxxxx

www.rsc.org/journalname

We present a molecular dynamics study of two polyelectrolyte gels with different degrees of ionization coupled in a slab geometry. Our simulations show that a pressure gradient emerges between the two gels that results in the buildup of a Nernst-Donnan potential. This methodology is reverse to experiments of the piezoionic or mechanoelectric effect, in which an electric potential gradient appears upon application of a pressure gradient to a hydrogel. The Nernst-Donnan potential at the interface is found to scale linearly with temperature with the coefficient of proportionality given by the fraction of concentrations of the uncondensed counterions. We show that the potential difference can also be expressed as a linear function of the lateral pressure, thus providing a molecular interpretation of the piezoionic effect.

1 Introduction

With increasing interest in motion capture, soft robotics, and wearable medical technologies, flexible, conductive, and biocompatible sensors are required[1–6]. Unfortunately, most materials currently available are either solid, as in electric wires, or liquid, as in battery electrolytes. Hydrogels are a promising class of materials that can potentially bridge the gap between current sensor technologies and tomorrow's soft-sensor requirements. On the molecular level, hydrogels resemble a three-dimensional network of polyelectrolyte chains that trap the conducting particles (ions). By choosing the monomers of the polyelectrolyte, one can program it to respond to external stimuli like temperature, pH or mechanical deformation (as in touch sensors). The appearance of an electrical voltage between different regions due to a non-uniform mechanical stress is called piezoionic or electromechanical effect[7–9]. To optimize the performance of hydrogels in touch sensors, one needs to understand in detail the motion of ions when pressure is applied.

Gels in dry form have a neutral backbone and have no macroions nor counterions. When placed in solvents, some monomers on the backbone dissociate and create pairs of charged macroions and floating counterions[2,10,11]. Several studies have addressed the appearance of an electrical potential between the gel immersed in a solvent and the solvent itself[12–17]. These studies found that gels with a negatively charged backbone (anionic gels) have an intrinsically negative electrical potential when compared to the surrounding solvent, as shown in Figure 1(A). This potential is called the Donnan potential, and it is a function of charge density along the polyelectrolyte backbone[12].

Sawahata et al.[2,9] found that an electrical potential could also be generated by a non-uniform compression of a gel. In a normal state, backbone molecules remain neutral and do not dissociate into positive and negative molecules. However, the authors argued that upon compression the monomers along the chains become more localized, and their entropy decreases as a result. When the entropic incentive becomes strong enough, molecules start dissociating, and the charge density increases. Non-uniform compression leads to a non-uniform generation of the dissociating charges and as a result, an electrical potential is generated between two parts of the gel, as shown in Fig. 1(B).

Another insight of the piezo-ionic effect was provided by Prudnikova et al.[12,18]. They noticed that when the ionization of a gel is kept constant (by putting the gel in a buffer solution), compression leads to an increase in the osmotic pressure of the gel, which leads to a separation of charges and hence to an increase of the electrostatic potential compared to a solution in equilibrium.

A complete understanding of the piezoionic effect is impossible without a full picture of the effect on the nanoscopic level. From experiments alone, it is difficult to gain insight into the ion behavior at the atomic scale. For example, it is a daunting task to independently manipulate solvent quality, the temperature of the solution, and polyelectrolyte ionization in a single experimental setup. Coarse-grained molecular dynamics (MD) simulations can be used to fill in the gap. MD simulations represent a bottom-up approach, where the behavior of each particle in the system is tracked, and collective properties are computed. Most importantly, MD simulations provide a simple framework to manipulate the parameters of the studied system and observe the results.

To date, most coarse-grained MD simulations of hydrogels were

[a] Dept. of Chemical Engineering, University of British Columbia, Vancouver BC Canada V6T 1Z4
[b] Dept. of Physics and Astronomy and Quantum Matter Institute, University of British Columbia, Vancouver BC Canada V6T 1Z1, email:jrottler@physics.ubc.ca

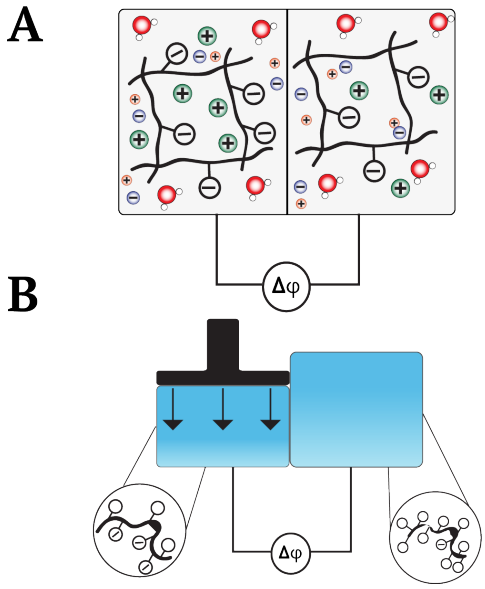

Fig. 1 A: A molecular picture of the Donnan equilibrium between two gels with different ionizations studied in experiments. Gels with a higher degree of negative backbone ionization have an intrinsically lower negative electrical potential when compared to the gels with lower degree of negative backbone ionization. The system consists of negative backbone ions (white), floating counterions (green), dissolved salt ions (orange and purple) and water molecules. B: A schematic representation of the explanation of the piezo-ionic effect proposed by Sawahata et al.[2,9] (see text).

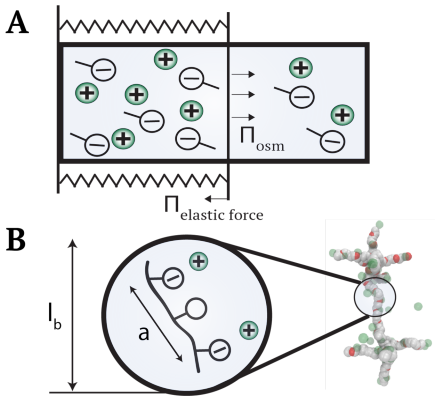

Fig. 2 A: Schematic representation of the interplay between the osmotic pressure Π_{osm} and elastic energy of the network Π_{el} in the Donnan equilibrium. B: Schematic illustration of counterion condensation. When the Bjerrum length l_B of the system becomes bigger than the distance between two neighboring backbone macroions $a \leq l_B$, the counterions become bound to the backbone ions and stop contributing to the osmotic pressure. The system consists of negative backbone ions (white), floating counterions (green).

performed in a setup with an ideal network of polyelectrolyte chains and explicit mobile counterions floating in an implicit solvent. Usually, the network consisted of a diamond or cubic lattice of crosslinking nodes connected by polyelectrolyte chains[11,19–32]. Despite its simplicity, such a setup already reveals interesting behavior. For instance, Yan et al.[33] demonstrated that at high temperatures and weak electrostatic interactions, the gel behaves as an ideal gas. In the limit of strong electrostatics and low temperatures, however, the authors found a somewhat counter-intuitive behavior, namely a decrease in pressure upon compression. This was attributed to counterion condensation. Erbas et al.[24,25] considered a gas of counterions sandwiched between two parallel gel slabs. They showed that the electrostatic energy changes upon compression of the gel at fixed strength of electrostatics, which could again only be explained by counterion condensation. Building upon the results of ref.[33], Mann and coworkers[27] performed an extensive study of gels of different sizes, ionizations, electrostatic strength, solvent qualities and other parameters. Their comparison between MD results with polyelectrolyte theory isolated different contributions to the overall pressure and validated the Manning theory of counterion condensation in the limit of straight polymer chains.

The works of Yan et al.[33] and Mann et al.[27] provide a comprehensive picture of a uniform gel under various conditions, while the work of Erbas et al.[24,25] provides insight into the behavior at the gel-counterion interface. The question arises how one could combine those studies and create a molecular dynamics setup that provides insight into the piezoionic effect. Inspired by the experimental work of Sawahata et al.[9], we consider here a gel slab consisting of two different degrees of ionization. Unlike the experimental setup, where ionization was induced by the lateral pressure applied to a gel, the ionization of both parts of the gel is different by design. When this system is allowed to equilibrate, an electric potential difference builds up at the interface, and the corresponding lateral pressure difference can be obtained. We analyze the ion density, potential and pressure profiles and show how they vary with temperature and ionization degree. We then show that the electrostatic potential for different gels can be collapsed onto a single master curve given by the classic expression for Donnan equilibrium. We finally show that the electrostatic potential is proportional to the lateral pressure difference between the two gels. The following part of the paper outlines fundamental theoretical principles that govern the piezoionic effect. Then, after describing the methodology, we will present our findings.

2 Theoretical concepts for polyelectrolytes

Many gels are well soluble in water due to an abundance of polar groups along their backbones. In the simplest representation, they consist of an elastic network of crosslinked polyelectrolytes. The elastic network comprises of both charged macroions and neutral monomers. The quantity of charged macroions depends on the degree of ionization f. Every charged macroion is compensated by an itinerant counterion to preserve electroneutrality.

It seems like counterions would favor to leave the hydrogel and escape into the external solvent as this would increase their translational entropy. However, this would break local electroneutrality. Thus, in case of an immovable gel network the counterions remain within the cell but exert an osmotic pressure onto the surroundings

$$\Pi^{osm}_{ideal} = k_B T \frac{N_{ci}}{V} = k_B T \frac{f N_m}{V}, \quad (1)$$

where N_{ci} and N_m are the number of counterions and monomers in the system. If the gel network is stretchable, the osmotic pressure swells the network. The stretching of the chains decreases their entropy, which creates an elastic pressure as illustrated in Fig. 2A. The elastic pressure produces mechanical work ΔW_{mech} due to the expansion of the network.

Besides the mechanical work, entropic forces could potentially break the electroneutrality of the system but only on small length scales $l < R_{ee}$, where R_{ee} is the average distance between any two crosslinking nodes. The breaking of electroneutrality produces an electrical potential $\Delta\varphi$, also called as Nernst-Donnan potential, which follows readily from equating the chemical potentials of the counterions of charge q inside and outside of the gel:

$$k_B T \ln(c_o/c_i) = q\Delta\varphi + \Delta\mu_{excess}, \tag{2}$$

where c_i and c_o are the average counterion concentrations inside and outside of the gel and μ_{excess} is the excess chemical potential due to excluded volume interactions present in the system.

At low temperatures, electrostatic interactions dominate over thermal energies and eq. (1) is no longer valid[2].The strength of the electrostatic interaction can be quantified via the Bjerrum length $l_B = k_{Coul} q^2/\varepsilon_{diel} k_B T$, where ε_{diel} is the dielectric permittivity of the medium, and k_{Coul} is the Coulombic constant. The Bjerrum length corresponds to the distance at which the Coulombic energy equals the thermal energy $k_B T$. According to Manning[34], when l_B becomes larger than the distance a between two consecutive charged monomers, all counterions become bound to their corresponding macroion in a phenomenon called counterion condensation as illustrated in Fig. 2B[27].

Additionally Manning's theory provides a simple expression for the effective ionization of the gel depending on it's temperature and, hence, the electrostatic strength[27] becomes

$$f_{eff} = \begin{cases} f & \text{, for } l_b < a \\ f/(l_b/(bf^{-\nu})) & \text{, for } l_b \geq a, \end{cases} \tag{3}$$

where ν is the Flory parameter and is assumed to be $3/5$.

3 Methods

Our simulation setup comprises of a box of 18x4x4 unit cells forming a cubic lattice of crosslinking nodes. The unit cells have lattice constant $l = 50\sigma$ and are connected by polyelectrolyte chains with $N_m = 100$ monomers. Due to the translational symmetry of the system there are three polymer chains per each cell with monomer number density $c = 3 \cdot 100/50^3 = 2.4 \cdot 10^{-3}\sigma^{-3}$. A fraction f of the monomers in each chain are ionized, i.e. they bear a negative charge $q = -1$. Monomers on the left side of the box are ionized with the ionization degree f_1, and monomers on the right side with the degree $f_2 > f_1$. After the network is created, N_{ci} counterions are inserted into the box at random positions to achieve electroneutrality. Monomers in the network are tethered to static nodes at the left and right boundaries of the simulation box. Periodic boundary conditions (PBC) are employed in lateral directions only. Reflective walls are put at $z = 0$ and $z = L_z$ to prevent atoms from escaping the box. Several snapshots illustrating the system are shown in Fig. 3.

The polyelectrolyte chains are modeled using the coarse-grained Kremer-Grest (KG) bead-spring model[35]. Excluded volume interactions are modeled via a purely repulsive Lennard-Jones (LJ) potential,

$$U^{LJ}(r_{ij}) = \begin{cases} 4\varepsilon \left[\left(\frac{\sigma}{r_{ij}}\right)^{12} - \left(\frac{\sigma}{r_{ij}}\right)^{6} - U(r_c) \right] & \text{,for } r < r_c \\ 0 & \text{,for } r \geq r_c \end{cases} \tag{4}$$

where $r_c = 2^{1/6}\sigma$. The Lennard-Jones parameters ε and σ correspond to the depth of the potential well and the distance at which the unshifted potential is zero, respectively. Both parameters are identical for all species present in the system (backbone monomers and floating counterions) and are used as units of energy and distance. Bonded interactions are modeled with a non-linear FENE potential,

$$U^{FENE}(r) = \begin{cases} -\frac{1}{2}\, k_f r_f^2\, \ln\left(1 - \left(\frac{r}{r_f}\right)^2\right) & \text{, for } r < r_f \\ \infty & \text{, for } r \geq r_f \end{cases} \tag{5}$$

with $k_f = 30\varepsilon/\sigma^2$, $r_f = 1.5\sigma$ resulting in a mean bond length of $b \sim \sigma$. Ions interact additionally via the Coulomb potential

$$U^{Coul}(r_{ij}) = k_{Coul} \frac{-q^2}{\varepsilon_{diel} r_{ij}} = -k_B T l_B / r_{ij}, \text{ for } r < r_c^{el}, \tag{6}$$

To reduce the computational cost, solvent molecules are treated implicitly through the dielectric constant ε_{diel}. To further optimize the computational performance, the electrostatic cutoff distance was set to $r_c^{el} = 17\sigma$, above which longer-range electrostatic interactions are calculated via a Particle-Particle-Particle Mesh (PPPM) Ewald solver for slab systems[36,37]. All simulations were performed in the NVT ensemble, with a timestep of integration $dt = 0.005$ and a PPPM accuracy of 10^{-4}. Molecular dynamics runs were performed using the LAMMPS code[38]. The MD trajectories were visualized using the VMD code[39] and analyzed using the MDAnalysis package[40,41]. The code base employed in the present work is summarized in the PyGels library[42]. All results are reported in reduced simulation units.

To calculate the pressure and energy profiles, the simulation box was divided into N_{bins} parts along the non-periodic z-direction. For every particle in a bin, an individual per-atom virial tensor σ_{ab}^i was calculated and averaged across each bin, where a, b could be any of x, y, z and i is the index of the particle. The per-atom virial tensor in the case of linear polymers with long-range Coulombic interactions is defined as:

$$\begin{aligned} \sigma_{ab} = -[& m v_a v_b + \frac{1}{2}\sum_{n=1}^{N_p} (r_{1_a} F_{1_b} + r_{2_a} F_{2_b}) + \\ & + \frac{1}{2}\sum_{n=1}^{N_b} (r_{1_a} F_{1_b} + r_{2_a} F_{2_b}) + \text{Kspace}(r_{i_a}, F_{i_b})] \end{aligned} \tag{7}$$

The first term is a kinetic energy contribution for the given atom.

The second term is a pairwise energy contribution, $\mathbf{r}_1$ and $\mathbf{r_2}$ are the positions of the two atoms in the pairwise interaction where N_p is the total number of neighbors, and $\mathbf{F}_1$ and $\mathbf{F}_2$ are the forces on the two atoms resulting from the pairwise interaction. The third term is a contribution from the covalent bonds, and the last term accounts for long-range Coulombic interactions. This tensor has units of energy and described in detail by Thomson et al.[43]. Two sets of pressure profiles were calculated during the simulation run. A lateral pressure profile via $P^{lat}(z) = -(\sigma^i_{xx} + \sigma^i_{yy})/2V^{z_j}_{bin}$ and the pressure component along the z axis $P^{zz}(z) = -(\sigma^i_{zz})/V^{z_j}_{bin}$. During the production run, the pressure profile was recorded every 500 steps and averaged in post-processing. The energy and concentration profiles were calculated in a similar fashion.

To perform the counterion condensation analysis we measured the distances between the gel monomers and counterions. If counterions were within $r_{cut} = 2\sigma$ of the gel backbone then it was considered to be condensed. The value of r_{cut} was chosen to include the first two peaks of the radial distribution function of the condensed ions. Counterions that were within r_{cut} of more than one backbone monomer were counted only once. The results for the fractions of the condensed atoms were time averaged across the simulation.

To calculate the electrostatic potential profiles, snapshots were saved every 1000 steps and imported into VMD's built-in PME Poisson solver[44]. The potentials of each snapshot were averaged to obtain a potential profile $\phi(z)$. These curves were fitted to

$$\phi(z) = \phi_0 + A \cdot \tanh(-x/x_0) \quad (8)$$

via the parameters x_0, ϕ_0, A. Eq. (8) arises from solving the Poisson equation in the geometry of two semi-infinite slabs with a potential at the interface ($\varphi(z-) = \varphi(z+)$).

4 Results

4.1 Three regimes of Donnan equilibrium

We begin our investigation of the piezoionic effect by analyzing a system with ionization degrees $f_1 = 0.1$ and $f_2 = 1.0$, i.e. 10% of monomers are ionized on the left and 100% on the right side. To gain insight into the conformation of the gel and counterions, several snapshots at three different temperatures $T = 1.1, 0.3, 0.1$ are shown in Fig. 3. A qualitative difference is observed in the behavior at high, medium and low temperatures. At high temperatures (regime 1), counterions float uniformly within the network. They exhibit high osmotic pressure and cause significant swelling. Due to the high degree of swelling, the boundary between two parts of the gel is pushed further left. As the temperature decreases to $T = 0.3$ the system transitions into regime 2. The particles on the left side of the box continue to behave as they did in regime 1, while the counterions on the right side undergo counterion condensation. Positively charged floating counterions become bound to the negatively charged backbone macroions. The bound counterions no longer contribute to the osmotic pressure, hence reducing the levels of swelling of the network. When the temperature becomes even lower (regime 3), counterions in both parts of the system condense and become bound to the backbone macroions. Since the fraction of the free-floating counterions is further reduced due to the condensation on both parts, the exerted osmotic pressure decreases even further. This causes significantly lower degrees of swelling than in the case of regime 1, as seen in Fig. 3

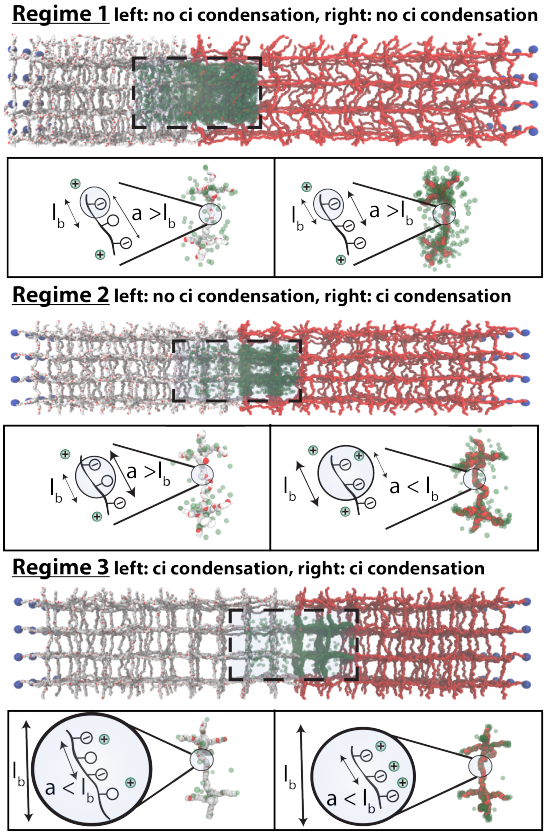

Fig. 3 Snapshots of a system with ionization degrees $f_1 = 0.1$ and $f_2 = 1.0$ at three temperatures $T = 1.1, 0.3, 0.1$. In snapshots white balls are: uncharged backbone monomers, red: negatively charged monomers, blue: tethered static monomers, green: positevely charged counterions. For illustration purposes, only counterions within the dashed box are shown. Regime 1: no counterion condensation, i.e. the Bjerrum length is smaller than the distance between two consecutive backbone charges. Regime 2: the left part (less ionized) of the system is not condensed, but the right part has undergone counterion condensation. Regime 3: both parts of the system undergo counterion condensation.

These trends can be rationalized with Manning criterion for counterion condensation. For the present gel, the spacing of charges in gel 1 is $a_1 = R_{ee}/N_m f_1 \simeq 5$, while $a_2 \simeq 1$. In regime 1, the Bjerrum length $l_B = 1/T = 0.91$ is smaller than both a_1 and a_2, hence no counterions condense. In regime 2, however, $l_B = 3.33$ exceeds a_2 but not a_1, so counterions condense in gel 3 only. Finally in regime 3, $l_B = 10$ exceeds both a_1 and a_2 and condensation occurs in both gels.

To quantify the counterion condensation, we performed a counterion condensation analysis as described above. In Fig. 4, we present the fraction of free counterions $f_{\text{free,i}} = f_i(1 - Q_i)$, where Q_i is the fraction of condensed ions. The theory predicts that at high temperatures no counterion condensation will occur and the effective ionization $f_{\text{free,i}}$ should remain equal to the actual ionization f_i. As the temperature is lowered, counterions are expected to condense, hence $f_{\text{free,i}}$ should decrease. As expected, we ob-

serve that the fraction of free counterions saturates at high temperatures, indicating that the electrostatic forces are not strong enough to facilitate condensation. Also, at a certain temperature (which depends on the ionization of the gel), the gel undergoes a transition where the effective ionization starts to decrease with decreasing temperature. The three regimes of the Donnan equilibrium introduced previously in Fig. 3 can also be observed depending on the onset of counterion condensation in each part of the simulation box. As the temperature decreases from T=1.1, where ions in both parts of the gel are not condensed, to T=0.7 the right side of the gel undergoes counterion condensation as indicated by the decreasing fraction of counterions, see 4 B and the system transitions from regime 1 to regime 2. When the temperature is further decreased to T=0.5, the counterions on the left side of the gel also condense, as indicated by the change in curve behavior in 4 A. The three regimes can also be observed on the graph of the ratio of effective ionization degrees $f_{free,2}/f_{free,2}$, see 4 B.

In Fig. 4, we also compare this effective ionization $f_{\mathrm{free,i}}$ that was calculated by directly analyzing the number of condensed counterions with the Manning prediction given by Eq. (3). The simulation curves are in a excellent agreement with this simple prediction in case of low ionization, however, the discrepancies increase in the case of higher ionizations (bottom panel). The discrepancies are possibly due to the fact that the Manning model was derived from solving a PB equation for a straight rod. However, in case of high ionization the system has numerous charged particles around the nodes, which have a star-topology rather than one of a straight chain.

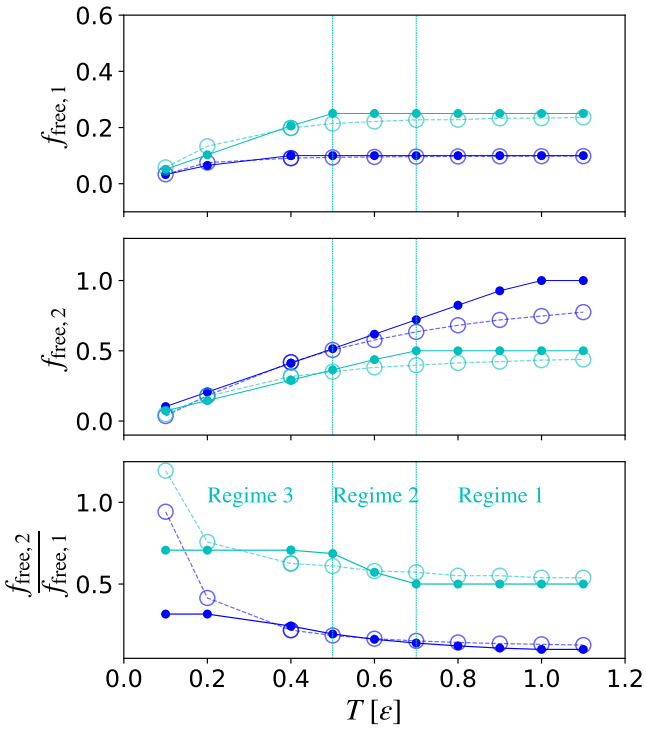

Fig. 4 Analysis of the fraction of free counterions (open symbols) compared to the Manning theory (filled symbols) for the gel slabs with ionization degrees $f_1 = 0.1$ and $f_2 = 1.0$ (blue) and $f_1 = 0.25$ and $f_2 = 0.5$ (cyan). A: Fraction of free counterions $f_{free,1} = f_1(1-Q_1)$ on the left side of the gel. B: Fraction of free counterions $f_{free,2} = f_2(1-Q_2)$ on the right side of the gel. C: Ratio $f_{free,2}/f_{free,1}$. Vertical dashed lines correspond to the temperatures where counterion condensation occurs in one part of the gel as indicated by the change in the curve behaviour.

4.2 Potential energies

The physical transition from regimes 1 to 3 shown in Fig. 3 also alters the potential energy profiles shown in Fig. 5. Here we plot the normalized profiles of the pair energy of interaction along the z-axis. We split the pair energy into Lennard-Jones (repulsion due to the excluded volume interaction) and Coulombic components. To be able to observe the qualitative changes in the energy of the system with temperature, the energy values were normalized by temperature. The energy profiles in Fig. 5 exhibit qualitatively different behavior across the three aforementioned regimes. In regime 1 (high temperatures $T = 1.1-0.5$), both the left and the right part of the normalized energy profiles show very little change with temperature and approach a common curve. In this regime, the energy is essentially proportional to temperature. In regime 2 (medium temperatures $T = 0.4-0.2$), the left part of the system shows no change with temperature, but the right one exhibits an increase in the value of the Lennard-Jones-component and a decrease in the Coulombic component. Finally, in regime 3 ($T = 0.1$), the energy profiles in both parts change. Instead of a evenly distributed gas of counterions, all counterions are now concentrated in the vicinity of the backbone ions. This drastically increases the repulsive Lennard-Jones component and decreases the Coulombic component of the energy.

4.3 Nernst-Donnan model for the electrostatic potential

In order to test whether the Nernst-Donnan picture describes the molecular simulations correctly, we first compute the ion concentration profiles in Fig. 6. With increasing temperature, the counterion profile becomes smoother as the itinerant ions equilibrate more easily across the system against the electrostatic energy penalty. We denote the concentrations in the two gels as c_1 and c_2, respectively. In order to systematically define these values in the two parts of the gel, we take the peak value of the concentrations away from any boundaries. Just as before, we introduce a value $c_{\mathrm{free,i}}$ which is a concentration of uncondensed counterions $c_{\mathrm{free,i}} = c_i(1-Q_i)$. Eq. (2) predicts that the potential scales linearly with temperature with the coefficient of the proportionality given by $\ln(c_{\mathrm{free,2}}/c_{\mathrm{free,1}})$. To test this, the potential energies $q\Delta\varphi$ of four different gels are scaled by $\ln(c_{\mathrm{free,2}}/c_{\mathrm{free,1}})$ and plotted as a function of temperature, see Fig. 7. All data sets collapse reasonably well onto a linear master curve with slope unity (circles).

Additionally, the master curve has zero offset along the vertical axis, with a slight divergence from linear behaviour at low temperatures. This confirms that excluded volume interactions and hence the excess chemical potential in Eq. (2) are negligible in the current model, especially in the high temperature regime.

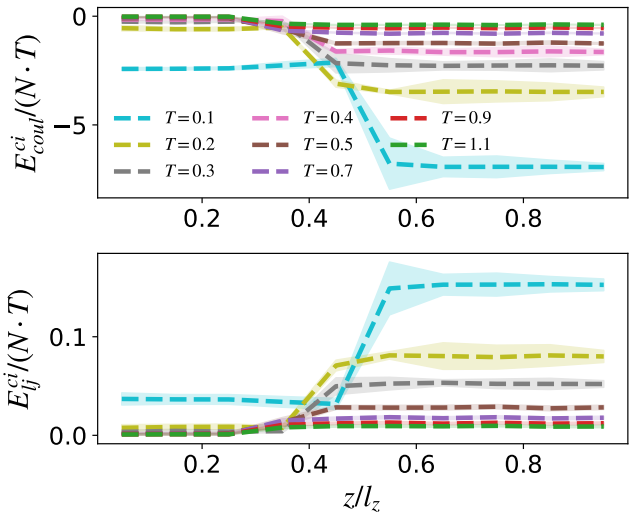

Fig. 5 Normalized energy profiles (A: Coulombic contribution, B: Lennard-Jones contribution) of the system with $f_1 = 0.1$, $f_2 = 1.0$ for different regimes. Here N is the total number of atoms in the system.

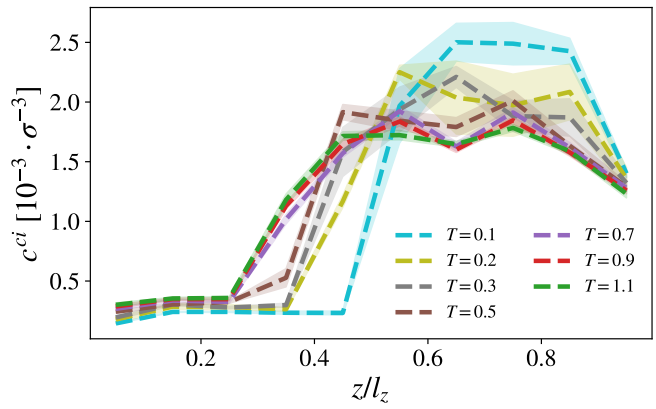

Fig. 6 Counterion concentration profiles of the system with $f_1 = 0.1$, $f_2 = 1.0$ for different temperature regimes. Colors are the same as in Fig. 5

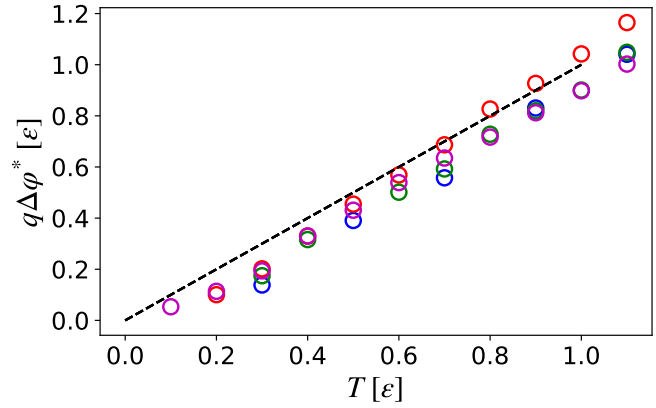

Fig. 7 Normalized electrostatic potential as a function of temperature. Circles: $q\Delta\varphi^* = q\Delta\varphi/\ln(c_{\mathrm{free},2}/c_{\mathrm{free},1})$. Red: $f_1 = 0.1$, $f_2 = 0.2$; magenta: $f_1 = 0.1$, $f_2 = 0.3$; green: $f_1 = 0.1$, $f_2 = 0.5$; blue: $f_1 = 0.1$, $f_2 = 1.0$. The dashed line has slope unity.

In experiments, the degree of ionization is not directly controlled, but is assumed to respond to external pressure changes. The electric potential can be connected to the applied pressure in two steps: understanding the behavior of the pressure profiles and then connecting the potential to the observed pressure difference between the two gels. To understand the behaviour of the pressure profiles at different temperatures, the pressure components P_{lat} and P_{zz} horizontal and vertical to the gel slab are computed as a function of the z-coordinate. The lateral pressure P_{lat} shows a step-like behavior with higher pressure on the higher ionized side, while P_{zz} remains constant across the gels as required by the condition of mechanical equilibrium. In Fig. 8, we plot the potential difference between the gel parts $q\Delta\varphi = q(\varphi_2 - \varphi_1)$ as a function of lateral pressure difference $P_{lat,2} - P_{lat,1}$. The figure shows that the data points fall nearly perfectly onto a straight line, especially at lower temperatures. The gels with higher ionization difference $f_2 - f_1$ exhibit higher pressure difference values and consequently higher potential values. This result shows that the energy of expansion scales linearly with the electrostatic energy change, which can also be inferred from the equality of chemical potentials that reads $\Delta P = \Delta\Pi$. Specifically, the minimum property of the Gibbs free energy that reads $V\Delta P = N\Delta\mu$, leads to $\Delta P \sim \Delta\Pi \sim c_{\mathrm{free},1} k_B T \ln(c_{\mathrm{free},2}/c_{\mathrm{free},1})$, which implies a linear scaling between pressure and Nernst potential when combined with $q\Delta\phi = k_B T \ln(c_{\mathrm{free},2}/c_{\mathrm{free},1})$ from Fig. 7.

5 Conclusions

Molecular dynamics simulations of coarse-grained polyelectrolyte gels have been performed to study the Donnan equilibrium and Nernst-Donnan potential at the boundary between gels with different ionizations. We explored several combinations of ionizations and different regimes of counterion condensation by varying the simulation temperature. The inspiration for the current study comes from the work of Sawahata et al.[9], who argued that the piezoionic (mechanoelectric) effect in gels arises from the stress-induced ionization of its compressed part, thus establishing a Nernst-Donnan equilibrium. Here, we showed that a reverse methodology can be used to study this electric potential: two gels with pre-defined ionization create a lateral pressure gradient that results in a the Nernst-Donnan potential generated at the interface.

Depending on the spacing between consecutive backbone macroions (a) and the Bjerrum length (l_B), different types of behavior could be observed. At high temperatures (small Bjerrum lengths $l_B < a_2 < a_1$), all counterions are itinerant. They exhibit high osmotic pressure, which creates high elastic pressure of the network which expands it and causes high degrees of swelling. Counterions float at random positions and the pair energy in the system scales linearly with temperature. The high osmotic pressure results in a relatively large break in the local electroneutrality, and hence large potential gradients occur at the interface between networks with different ionizations.

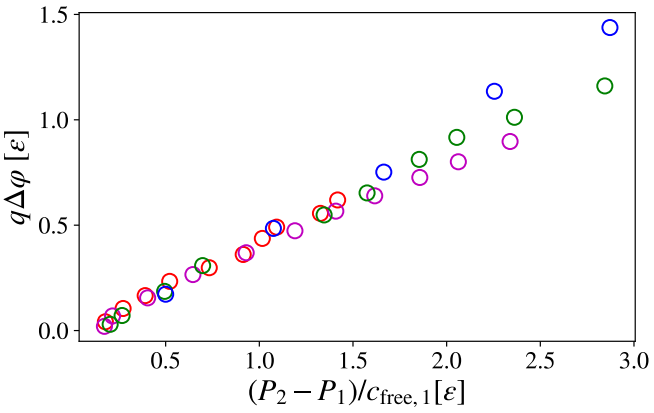

Figure 8 Potential difference as a function of the lateral pressure difference. Red: $f_1 = 0.1$, $f_2 = 0.2$; magenta: $f_1 = 0.1$, $f_2 = 0.3$; green: $f_1 = 0.1$, $f_2 = 0.5$; blue: $f_1 = 0.1$, $f_2 = 1.0$. Here V is the volume of the simulation box.

At low temperatures (high Bjerrum lengths $l_B > a_1, a_2$) both sides of the gel undergo counterion condensation. Positively charged floating counterions on the right side become bound to negatively charged backbone macroions. The bound counterions effectively stop contributing to the osmotic pressure, which causes smaller levels of swelling of the network on the right hand side. Both parts of the system experience a decrease in Coulombic energy and an increse in Lennard-Jones energy.

The Nernst-Donnan potential at the interface scales linearly with temperature with the coefficient of proportionality driven by the fraction of concentrations of the uncondensed counterions $\ln(c_{\mathrm{free},2}/c_{\mathrm{free},1})$. We also showed that the potential difference can be expressed as a linear function of the lateral pressure. Interestingly, this relationship is robust and hold equally well for weak and strong counterion condensation. This linear relationship thus provides a molecular level explanation of the piezoionic effect, and calls for verification in experiments.

6 Acknowledgement

The authors would like to acknowledge Felix Blyakmann, Yuta Dobashi, Alexei Dobrynin, Aykut Erbas, John Madden, and Saquib Sarwar for valuable discussions and feedback. This research was supported in part by a University of British Columbia Four Year Fellowship, in part by Compute Canada (www.computecanada.ca) and in part by the National Science Foundation under Grant No. NSF PHY11-25915.

References

1 M. C. Stuart, W. Huck, M. M. Genzer, C. Ober, M. Stamm, G. Sukhorukov, I. Szleifer, V. Tsukruk, U. Marek, F. Winnik, S. Zauscher, I. Luzinov and S. Minko, *Nature Materials*, 2010, **9**, 101–113.

2 Y. Osada and A. R. Khokhlov, *Polymer gels and networks*, 2002.

3 C. Laschi, B. Mazzolai and M. Cianchetti, *Sci. Robot.*, 2016, **1**, 3690.

4 M. Amjadi, K.-U. Kyung, I. Park and M. Sitti, *Advanced Functional Materials*, 2016, **26**, 1678–1698.

5 E. CalÃş and V. V. Khutoryanskiy, *European Polymer Journal*, 2015, **65**, 252 – 267.

6 M. S. Sarwar, Y. Dobashi, C. Preston, J. K. Wyss, S. Mirabbasi and J. D. W. Madden, *Science advances*, 2017, **3**, e1602200.

7 M. S. Sarwar, Y. Dobashi, E. Glitz, M. Farajollahi, S. Mirabbasi, S. Naficy, G. M. Spinks and J. D. Madden, Electroactive Polymer Actuators and Devices (EAPAD) 2015, 2015, p. 943026.

8 Y. Dobashi, M. S. Sarwar and J. D. W. Madden, *MRS Advances*, 2016, 1.

9 K. Sawahata, J. P. Gong and Y. Osada, *Macromolecular Rapid Communications*, 1995, **16**, 713–716.

10 M. Rubinstein and R. H. Colby, *Polymer physics*, 2003.

11 A. Vagias, P. Košovan, C. Holm, H. Butt, K. Koynov and G. Fytas, *Progress in Colloid and Polymer Science*, 2013, **140**, 53–62.

12 K. Prudnikova and M. Utz, *Macromolecules*, 2012, **45**, 1041–1045.

13 K. Prudnikova and M. Utz, *Macromolecules*, 2010, **43**, 511–517.

14 F. A. Blyakhman, A. P. Safronov, A. Y. Zubarev, T. F. Shklyar, O. A. Dinislamova and M. T. Lopez-Lopez, *Sensors and Actuators A: Physical*, 2016, **248**, 54–61.

15 T. F. Shklyar, A. P. Safronov, O. A. Toropova, G. H. Pollack and F. A. Blyakhman, *BIOPHYSICS*, 2011, **55**, 931–936.

16 F. Gao, F. B. Reitz and G. H. Pollack, *J. Appl. Polym. Sci.*, 2003, **89**, 1319–1321.

17 H. Guo, T. Kurokawa, M. Takahata, W. Hong, Y. Katsuyama, F. Luo, J. Ahmed, T. Nakajima, T. Nonoyama and J. P. Gong, *J.Chem. Phys.*, 2016, **49**, 3100–3108.

18 K. Prudnikova and M. Utz, *Frontiers in Sensing*, Springer Vienna, 2012, pp. 351–361.

19 S. Schneider and P. Linse, *European Physical Journal E*, 2002, **8**, 457–460.

20 S. Schneider and P. Linse, *The Journal of Physical Chemistry B*, 2003, **107**, 8030–8040.

21 S. Schneider and P. Linse, *Macromolecules*, 2004, **37**, 3850–3856.

22 F. a. Escobedo and J. J. de Pablo, *Physics Reports*, 1999, **318**, 85–112.

23 F. A. Escobedo and J. J. de Pablo, *Molecular Physics*, 1997, **90**, 437–444.

24 A. Erbas and M. Olvera de la Cruz, *Macromolecules*, 2016, **49**, 9026–9034.

25 A. Erbas and M. Olvera de la Cruz, *ACS Macro Lett.*, 2015, **4**, 857–861.

26 S. Edgecombe, S. Schneider and P. Linse, *Macromolecules*, 2004, **37**, 10089–10100.

27 B. A. Mann, *PhD thesis*, Johannes Gutenberg-Universität, Mainz, 2005.

28 K. Saalwächter, F. Kleinschmidt and J. U. Sommer, *Macromolecules*, 2004, **37**, 8556–8568.

29 P. Košovan, T. Richter and C. Holm, *Macromolecules*, 2015, **48**, 7698–7708.

30 M. Quesada-Pérez, J. Guadalupe Ibarra-Armenta and A. Martín-Molina, *The Journal of chemical physics*, 2011, **135**, 094109.
31 M. Quesada-Pérez, J. Ramos, J. Forcada and A. Martín-Molina, *The Journal of chemical physics*, 2012, **136**, 244903.
32 M. Quesada-Pérez, S. Ahualli and A. Martín-Molina, *Journal of Polymer Science, Part B: Polymer Physics*, 2014, 1403–1411.
33 Q. Yan and J. J. de Pablo, *Physical review letters*, 2003, **91**, 018301.
34 G. S. Manning, *Biophysical Chemistry*, 1977, **7**, 95–102.
35 K. Kremer and G. S. Grest, *Journal of Physics: Condensed Matter*, 1990, **2**, SA295–SA298.
36 I.-C. Yeh and M. L. Berkowitz, *The Journal of Chemical Physics*, 1999, **111**, 3155–3162.
37 R. Hockney and J. Eastwood, *Computer Simulation Using Particles*, Taylor & Francis, 1988.
38 S. Plimpton, *Journal of Computational Physics*, 1995, **117**, 1–19.
39 W. Humphrey, A. Dalke and K. Schulten, *Journal of Molecular Graphics*, 1996, **14**, 33–38.
40 M. Khoshlessan, I. Paraskevakos, S. Jha and O. Beckstein, Proceedings of the 16th Python in Science Conference, 2017.
41 N. Michaud-Agrawal, E. J. Denning, T. B. Woolf and O. Beckstein, *Journal of Computational Chemistry*, 2011, **32**, 2319–2327.
42 V. Triandafilidi, *https://github.com/bazilevs31/pygels*, 2013.
43 A. P. Thompson, S. J. Plimpton and W. Mattson, *The Journal of chemical physics*, 2009, **131**, 154107.
44 A. Aksimentiev and K. Schulten, *Biophysical Journal*, 2005, **88**, 3745–3761.